Nanomed. J. 10(4): 279-292, Autumn 2023

RESEARCH PAPER

Enhanced efficiency of samarium-doped TiO_2 nanoparticles for targeted imaging: Characterization and *in vivo* evaluation

Wesam Abd ElKader [1], Raghda AboGabal [2]*, Amr Abdelghany [3], Ahmed Oraby [1]

[1]Physics Department, Faculty of Science, Mansoura University, Mansoura, Egypt
[2]Mansoura Urology and Nephrology Center, Mansoura University, Mansoura 35516, Egypt
[3]Spectroscopy Department, Physics Division, National Research Center, 33 ElBehouth St., Dokki, 12311, Cairo, Egypt

ABSTRACT

Objective(s): This study aimed to synthesize Samarium-doped TiO_2 nanoparticles (Ti(Sm)O_2 NPs) using solvothermal synthesis and evaluate their suitability as targeted imaging agents. The objectives were to enhance the stability and biocompatibility of the nanoparticles by coating them with polymeric materials and assess their imaging capabilities and safety.

Materials and Methods: Ti(Sm)O_2 NPs were synthesized using the solvothermal method with TiO_2, NaOH, and deionized water. The resulting solution was filtered, dried, and processed in a Teflon-lined stainless steel autoclave. The obtained product was washed, dried, and coated with FDA-approved polymers including polyethylene glycol (PEG), polyvinylpyrrolidone (PVP), and carboxymethyl cellulose (CMC). Coating was achieved through a mixing process and subsequent drying.

Results: Characterization studies confirmed the desired morphology, crystal structure, optical properties, surface charge, and biocompatibility of the Ti(Sm)O_2 NPs. *In vivo* imaging evaluations demonstrated their excellent imaging capabilities, particularly in distinguishing lung pathologies. Additionally, *in vivo* toxicity studies confirmed the nanoparticles biocompatibility and safety, with no adverse effects on organ function observed.

Conclusion: In this study, Samarium-doped TiO_2 nanoparticles WERE successfully synthesized and their potential as targeted imaging agents was evaluated. The coating of the nanoparticles with polymeric materials enhanced their stability and biocompatibility. The nanoparticles exhibited excellent imaging capabilities, particularly in distinguishing lung pathologies. Moreover, they demonstrated biocompatibility and safety *in vivo*. These findings contribute to the development of advanced contrast agents for biomedical applications, providing effective tools for targeted imaging and improving the diagnosis and monitoring of various lung pathologies.

Keywords: *Biopolymers, Contrast media, Drug-related side effects and adverse, Polyethylene glycols, Samarium, Titanium dioxide, X-rays*

How to cite this article

Abd ElKader W, AboGabal R, Abdelghany A, Oraby A. Enhanced efficiency of samarium-doped TiO_2 nanoparticles for targeted imaging: Characterization and in vivo evaluation. Nanomed J. 2023; 10(4): 279-292. DOI: 10.22038/NMJ.2023.72742.1785

INTRODUCTION

The versatility of nanomaterials in performing multiple functions has greatly facilitated their widespread use in the field of cancer imaging, diagnosis, and treatment [1]. Accurate diagnosis of diseases often requires comprehensive information that cannot be obtained through a single imaging modality alone. As a result, multi-modal imaging systems have emerged as a promising approach for highly efficient cancer theranostics. In recent years, X-ray computed tomography (CT) has witnessed significant advancements in its core technology and innovative therapeutic applications. However, the development of clinical X-ray contrast agents has seen limited progress in the past few decades. There is a need to overcome challenges such as achieving high concentration in the bloodstream, maintaining stable concentration over time, and enhancing aggregation at specific regions of interest. Addressing these challenges is crucial for improving the performance and efficacy of CT imaging, ultimately advancing the diagnosis and treatment of cancer [2].

The limitations of conventional iodine-based X-ray contrast agents used in CT imaging, such

* *Corresponding author: Email: raghdaabogabal@gmail.com,*
Note. This manuscript was submitted on April 10, 2023; approved on June 15, 2023

as rapid blood clearance, have prompted the exploration of alternative solutions. In recent years, there has been growing interest in the development of nanoparticle-based contrast agents to address these limitations [3]. Nanoparticulate probes offer several advantages over single molecule-based agents, including the ability to integrate different contrast-generating materials, longer circulation time in the bloodstream, and higher payload capacity. This review highlights the significance of nanoparticle-based contrast agents in medical imaging, particularly in the context of CT imaging, and their potential to enhance imaging performance and capabilities [4]. By leveraging the unique properties of nanoparticles, researchers aim to overcome the challenges associated with conventional contrast agents and improve the accuracy and quality of CT imaging for various medical applications.

Gold nanoparticles (AuNPs) show promise as iodine-free X-ray contrast agents in medical applications [5]. Gold's unique properties, including its higher nuclear number, K-edge, and mass X-ray absorption coefficient compared to iodine, make it an attractive alternative. AuNPs provide 2.7 times greater X-ray contrast per unit weight than iodine and exhibit optimal X-ray absorption in the 80-100 keV range, enabling improved visualization of blood vessels [6]. Moreover, AuNPs have demonstrated excellent biocompatibility and low toxicity, rendering them suitable for a range of biological applications [7].

Bismuth (Bi), a metal with a high nuclear number (ZBi=83), has gained interest as a potential alternative to iodine-based X-ray contrast agents due to its low toxicity and diverse applications in medicine, cosmetics, and surgery. Bismuth salts were among the earliest contrast agents used in X-ray imaging of patients [8]. Coated bismuth nanoparticles were introduced as injectable contrast agents for CT imaging in mice, demonstrating prolonged circulation compared to iodine-based agents [9]. Bismuth-enhanced nano-colloids have also been utilized as contrast agents for spectral CT molecular imaging to visualize thrombus [10]. However, due to their high cost and adverse effects, high doses of bismuth compounds were eventually replaced by more cost-effective alternatives. This review highlights the potential of bismuth as an X-ray contrast agent, its early applications, and the challenges in its widespread use.

In the early 1970s, tantalum nanoparticles (NPs) were investigated as a contrast agent for bronchography. However, compared to iodine, tantalum had a limited contrast impact, especially at high X-ray voltages [11]. *In vivo* studies in mice demonstrated the absence of immediate or harmful effects, and the NPs were eliminated through renal clearance without adverse effects. More recently, Hyeon and colleagues developed a microemulsion strategy to synthesize uniform-sized TaOx particles in large quantities, opening up new possibilities for their application as contrast agents. This review highlights the historical usage of tantalum NPs in bronchography, their contrast properties, and the latest advancements in their synthesis for potential medical imaging applications [12].

Lanthanide elements, such as gadolinium and ytterbium, have shown significant potential for use in X-ray scanning techniques. These elements possess higher nuclear numbers than iodine, resulting in increased X-ray attenuation and enhanced contrast in poly-spectrum imaging. Gadolinium, in particular, exhibits a higher K-edge (52 keV) compared to iodine, leading to more pronounced X-ray attenuation and superior contrast. Ytterbium, among the lanthanide elements, stands out as a promising candidate for diagnostic and molecular imaging applications due to its excellent biocompatibility and high mass X-ray absorption coefficient [8]. Among the lanthanide elements, ytterbium is the most promising contender for diagnostic and molecular imaging applications due to its excellent biocompatibility and high mass X-ray absorption coefficient (3.88 $cm^2 g^{-1}$ at 100 keV) [13].

Titanium Dioxide (TiO_2) nanoparticles have gained significant attention as a semiconductor material due to their high photochemical stability and cost-effectiveness [14]. To optimize their radiosensitizing effects, doping TiO_2 nanoparticles with high Z elements while preserving their fundamental physical properties has been explored [15]. In this regard, the incorporation of Samarium (Sm) into TiO_2 nanoparticles has been investigated, resulting in enhanced efficiency. These $Ti(Sm)O_2$ nanoparticles, immobilized with polyethylene glycol (PEG) and fluorescent dye, offer a multifunctional platform for X-ray computed tomography (CT) and fluorescence imaging. Notably, $Ti(Sm)O_2$ nanoparticles exhibit desirable characteristics such as biocompatibility, antimicrobial properties, high chemical stability, specific surface area, and catalytic activity. This review highlights the potential of $Ti(Sm)O_2$ nanoparticles and their unique properties for

various biomedical applications, including imaging and therapeutic interventions [2].

The surface characteristics of nanoparticles (NPs) play a crucial role in their biomedical applications, influencing their interactions within the human body. Coatings on NPs can provide protection against mononuclear phagocyte and protein adsorption in vivo, thereby maintaining their stability. However, creating a surface coating material that offers colloidal stability and biocompatibility under physiological conditions is a significant challenge [16]. The choice of coating agent and its interaction with the biological environment determine the stability and biocompatibility of NPs [17]. Different classes of coating substances, such as synthetic and natural hydrophilic polymers like poly(ethylene glycol) (PEG), poly(vinyl alcohol) (PVA), and poly(L-lysine) (PLL), have been investigated for their potential in biomedical applications [18, 19]. These coatings have shown benefits such as enhanced colloidal stability, reduced cytotoxicity, and improved biocompatibility of various NPs, including iron oxide and titanium dioxide nanoparticles [20]. One common class of compounds are synthetic and natural hydrophilic polymers such as poly(ethylene glycol) (PEG) which modified USPIONs synthesized [20], and poly(vinyl alcohol) (PVA), which shows superparamagnetic, hydrophilic properties and may serve as a potential candidate for biomedical applications [21], poly (L-lysine) (PLL) which provide good colloidal stability for Iron Oxide and modified nanoparticles less than 10 nm in diameter were tested for cell labelin [22]. Mano et al. found that modifying TiO_2 NPs with PEG reduces their cytotoxicity and the induction of stress-related genes [23]. This study aims to enhance the imaging capabilities of titanium dioxide (TiO_2) nanoparticles (NPs) by incorporating lanthanides and improving their physical and biological properties. By coating these NPs with polymers, they can be used as safe and biocompatible X-ray computed tomography (CT) contrast agents *in vivo*. The findings of this study demonstrate the potential applications of lanthanide-doped TiO_2 NPs and other multifunctional nanoparticles in cancer diagnostics and therapy. These results underscore the importance of harnessing the unique properties of lanthanide-doped TiO_2 NPs for advanced imaging techniques and their potential significance in cancer research and treatment.

MATERIALS AND METHODS

Materials

Titanium dioxide (TiO_2 =79.89 g, Min. assay (ex Ti) 99%, Max. limits of impurities, loss on drying .5 %, Iron (Fe) .05%). Sodium hydroxide (Sodium hydroxide pellets AR assay 99.5 %, MW.40.00, SO. 55592, Egypt). Carboxy Methyl (CMC), Carmellose Sodium, assay: 99.5% pure Na-CMC, maximum .5 salt, pH: 6.5:8.5, pure, M.W. =700.000, Denisity:1.59 g/cm^3, soluble in water, loss on drying max. 10%. PolyVinylPyrrolidone(PVP), (K-30), pure, M.W. =40.000, MUMBAI, INDIAN. Polyethene glycol 6000 (PEG6000), M.W: 950-1,050, soluble in water, Density: 3.58 g/cm^3. Samarium (III) nitrate hexahydrate, 99.9% (REO), Hygroscopic. Store under Nitrogen, 10 g, LOT: D12X008, FW:444.45, Germany. All the aqueous solutions are prepared using triple distilled deionized water (DW).

Synthesis of TiO_2 NPs

TiO_2 nanoparticles were synthesized using the hydrothermal method. Initially, a solvent mixture was prepared by combining 5 g of TiO_2 and 4.8 g of NaOH in 60 ml of deionized water at room temperature. The mixture was stirred for 3 hr at 60 °C, resulting in a clear solution. To achieve a pH of 7, filtration using filter papers was performed. The solution was then dried at 60 °C. The dried solution was magnetically stirred and transferred to a 100 ml Teflon-lined stainless steel autoclave, which was heated to 150 °C for 3 hr. After cooling to room temperature, the obtained product was washed five times with pure ethyl alcohol and distilled water. The resulting white precipitate was dried overnight at 60 °C and subsequently calcined at 500°C for 2 hr.

Synthesis of 1% Samarium-doped TiO_2 NPs ($Ti(Sm)O_2$-NPS)

To synthesize the $Ti(Sm)O_2$ nanoparticles, Samarium (III) nitrate hexahydrate was added to the mixture. Following the hydrothermal method mentioned earlier, the preparation involved the use of ethanol, HCl, and deionized water. Specifically, a solution was created by mixing 30 ml of ethanol, 0.5 ml of HCl, 2 ml of deionized water, and 1% samarium. Under stirring, 5 ml of titanium oxides were added drop by drop to the solution and vigorously stirred for 15 min, following the same procedure as described previously.

Synthesis of polymer encapsulated TiO_2 and Samarium doped TiO_2NPs

To enhance the stability of the CT contrast agents, we implemented three surface modifications on the nanoparticles (NPs). The NPs were designed with a core-shell structure, where the NP core comprised multiple CT-dense nanocrystals (NCs), and the

shell was formed using FDA-approved polymers: polyethylene glycol (PEG), polyvinylpyrrolidone (PVP), and carboxymethyl cellulose (CMC). To carry out the surface modification, a solution containing 0.1 g of TiO_2 NPs and 0.1 g of each polymer (PEG, PVP, and CMC) was mixed in 100 ml of deionized water. The mixture was then stirred at 60 °C for 3 hr. Subsequently, the solutions were separated through centrifugation at 60 rpm for 2 min, and the resulting NPs were dried at 60 °C.

Characterization techniques

The optical properties of the synthesized nanoparticles (NPs) were characterized using a UV-Vis spectrometer (Pg instruments, T80+, UV/Vis spectrometer, China). Absorbance spectra measurements were performed in the wavelength range of 200-900 nm to investigate the optical properties of the NPs. This range encompasses the UV, visible, and near-infrared regions of the electromagnetic spectrum, where electronic transitions occur. Molecules with bonding and non-bonding electrons (n-electrons) can absorb energy from ultraviolet or visible light, causing them to be excited to higher anti-bonding molecular orbitals. The UV/Vis spectroscopy provides valuable insights into the electronic transitions and optical behavior of the NPs [24].

The functional groups present in the synthesized TiO_2 nanoparticles (NPs) were identified using Fourier transform infrared (FT-IR) spectroscopy. The FTIR spectra were collected using an FTIR spectrophotometer (PerkinElmer-99075, Germany) employing the standard KBr pellet technique. The spectral range analyzed was 4000 - 450 cm^{-1}, with a resolution accuracy of 4 cm^{-1}. FT-IR spectroscopy is a powerful technique that enables the characterization and identification of various functional groups present in the NPs, providing valuable information about the chemical composition and structure of the synthesized TiO_2-NPs.

Transmission electron microscopy (TEM) imaging was performed using a JEOL JEM-2100 instrument from Japan, equipped with a CCD camera. To prepare the samples for TEM measurements, a wax plate was covered with a copper grid, and a diluted nanosuspension was sprayed onto the surface of the grid [25]. This ensured that the nanostructures formed in the colloids were visualized under the TEM. The obtained TEM images provided high-resolution details of the nanoparticles and their morphology. Additionally, the size distribution of the nanoparticles was analyzed using ImageJ 64-bit software (version ij 153-win-java 8), and a size distribution histogram was generated to estimate the particle size range and distribution.

The zeta potential of the nanoparticles was determined using a zeta potential analyzer and particle sizing devices at a temperature of 25 degrees Celsius. The specific instrument used for this analysis was the Malvern Zetasize Nano-zs 90 from the USA. The zeta potential measurement provides information about the surface charge of the nanoparticles. When particles have a high negative or positive zeta potential, they tend to repel each other, leading to a stable colloidal suspension with no flocculation. Conversely, particles with low zeta potential values lack the repulsive force necessary to prevent their collision and flocculation. According to the principle of electrophoresis, nanoparticles with zeta potentials exceeding +30 mV or falling below -30 mV are considered to be colloidal and exhibit stability (Franks, 2002). The zeta potential analysis helps assess the stability of the nanoparticles and their potential for aggregation or dispersion in solution [26].

Luminescence qualities were assessed using a spectrofluorometer (Jasco FP-6500, Japan) and two-photon laser confocal microscopy (690–1040 nm) (Xenon arc Lamp 150 watt). The excitation and emission spectra were used to analyze the nanocomposite's luminescence capabilities. Before measurement, the nanocomposite is purified by dialysis against distilled water for one week, and the purified samples are distributed in distilled water [19].

Cytotoxicity and cell viability assay

In the cytotoxicity and cell viability assay, peripheral mononuclear cells (PBMC) were isolated from whole blood using density centrifugation with Ficoll-Paque. The procedure involved centrifuging Hanks balanced salt solution (HBSS) with heparinized human blood, collecting the upper fraction containing PBMCs, and resuspending the cells in PBS buffer. Cell counting was performed using a hemocytometer and the trypan blue exclusion method. The isolated PBMCs were then seeded in a 96-well plate with a culture medium and incubated at 37 °C with 5% CO_2. For cell characterization, PBMCs at passage three were analyzed by flow cytometry using anti-CD45 PE antibody [27]. The cells were stained, and data analysis was performed using a flow cytometer. To assess cell viability and cytotoxicity of the nanoparticles, cells were seeded in a 96-well plate and incubated with the nanoparticles for a specific duration. After incubation, trypan blue was added to each well, and the plates were further

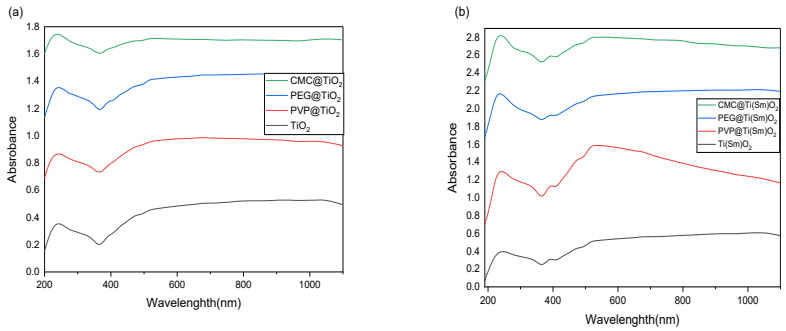

Fig. 1. (a) UV spectra of TiO_2, PVP@TiO_2, PEG@TiO_2, and CMC@TiO_2 nanoparticles (b) UV spectra of Ti(Sm)O_2, PVP@Ti(Sm)O_2, PEG@ Ti(Sm)O_2, and CMC@Ti(Sm)O_2 nanoparticles

incubated and placed on a shaker to facilitate cell-NP interaction. Cell morphology was assessed by capturing photographs of living cells' interaction with different nanoparticles These experimental procedures, as described by Gabal *et al.*, allowed for the evaluation of cytotoxicity and cell viability using peripheral mononuclear cells. The isolation and characterization of PBMCs provided a standardized cell population for the assessment, and the incubation with nanoparticles allowed for the observation of any potential effects on cell viability and morphology [28].

Assessment of the toxicity and safety profile

The study was conducted on 51 male mice weighing 29–40 g. They were obtained from the animal house of MERC, the faculty of medicine, Mansoura University, and after approval by our local ethical committee. Considering that accumulation of NPs in vivo might stimulate toxicity or adverse side effects after long-term treatment, we next evaluated the potential long-term toxicity of NPs *in vivo*. Animal Model The mice were randomly allocated into two groups (24 rats each) and three control: The control group was injected with saline only; after intravenous injection(iv) of NPs, mice were sacrificed after 3hrs and 7 days, major organs (liver, heart, Lung, spleen, Pancreas, and kidneys) were collected for H&E staining. samples were then fixed in 10% formalin, followed by routine dehydration, immersion, and paraffin embedding. They were sectioned into 4-µm-thick slices for hematoxylin and eosin staining and examined by light microscopy. Degenerative changes were observed and graded into absent, defined as no obvious pathological changes; mild, defined as focal pathological changes; or marked, defined as diffuse pathological changes, as modified from a previous report. Blood biochemistry analyses were performed, and Blood samples were also collected to investigate nephrotoxicity and hepatotoxicity. Aspartate aminotransferase, alanine aminotransferase, and Creatinine levels were determined after 1 hr and 6 days of treatment in serum samples collected. Levels of ALT and AST refer to liver damage. A measurement of the serum creatinine level is often used to evaluate kidney function.

***In vitro* phantom imaging**

For in vitro phantom measurements, solutions of TiO_2 and Samarium doped TiO_2 were prepared at various concentrations (6.25, 12.5, 25.0, 50.0, and 100.0 mM) diluted in DW in 1.0 ml microtubes. Phantom CT images were acquired on a Toshiba Alexion CT scanner operating at 80, 100, 120 kVp, and 22, 30, 37 µA, respectively, with a slice thickness of 0.5mm and gantry rotation time of 0.6 S. Images were analyzed using J-image 64-bit (ij 153-win-java 8). Create a circular region of interest (ROI) over each tube, and the attenuation and standard deviation were recorded for each ROI analyzed [29]. From these values, the Contrast rates were calculated for different image sets via the following equation:

$$Contrast = \frac{I_{max} + I_{min}}{I_{max} - I_{min}}$$

RESULTS AND DISCUSSION

UV/Visible optical absorption spectral data

The study involved recording ultraviolet-visible (UV/Vis) absorbance spectra to evaluate the electronic structure and optical band gap of the nanoparticles (NPs). The UV/Vis spectra of pure Titanium dioxide (TiO_2) nanoparticles and Samarium-doped TiO_2 nanoparticles were obtained and analyzed. In Fig. 1a, the absorbance peak at 364.23 nm corresponds to the presence of TiO_2 in the sample. In Fig. 1b, two absorption peaks

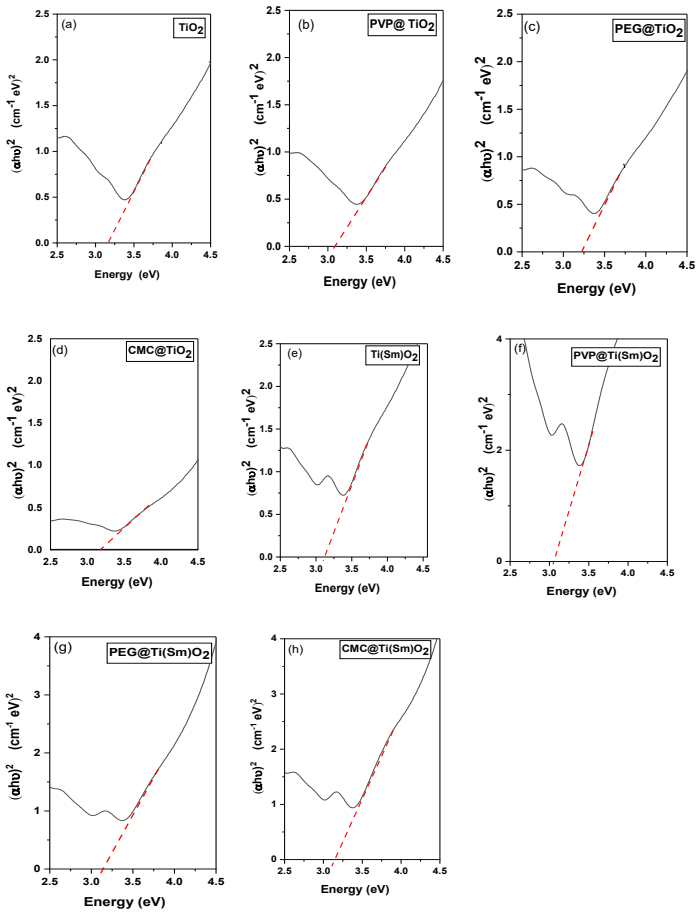

Fig. 2. Energy gap of (a) TiO_2, (b) PVP@TiO_2, (c) PEG@TiO_2, (d) CMC@TiO_2, (e) Ti(Sm)O_2, (f) PVP, (g) PEG@Ti(Sm)O_2, (h) CMC@Ti(Sm)O_2 nanoparticles

are observed for Samarium-doped TiO_2 at 366.65 nm and 409.2 nm, with the latter attributed to the presence of Samarium. The specific absorption characteristics may vary with different polymeric precursors used in the synthesis process. The absorption edge in the UV region represents electronic transitions from the occupied valence band to the empty conduction band. Absorption occurs when the energy of the incident photon matches or exceeds the band gap energy of the material. The indirect energy gap (Eg) was estimated using the equation αhυ=A(hυ−Eg)2, where α, h, and υ represent the absorption coefficient, Planck's constant, and frequency of the incident photon, respectively. To determine the band gaps, plots of (αhυ)2 versus (hυ) were generated, and the linear portions of the resulting curves were extrapolated to the x-axis (zero absorbance) as shown in Fig. 2. The band gaps (Eg) were evaluated to be in the range of 3.4 to 2.8 eV for the as-prepared TiO_2 samples containing various polymers such as PEG, PVP, and CMC. The addition of polymers to TiO_2 NPs resulted

Table 1. Characterization of TiO_2 nanoparticles.

Sample	Zeta potential (mv)	Conductivity (ms/cm)	Energy gap (eV)	Particle size (nm)
TiO_2	-61.5±18	3.16	3.15	70.5±23
PVP@TiO_2	-37.9±9	0.99	2.95	
PEG@TiO_2	-49.8±9	2.2	3.23	
CMC@TiO_2	-38.27±11	2.2	2.16	
Ti(Sm)O_2	-61.6±7.33	2.5	3.10	83.03±22
PVP@ Ti(Sm)O_2	-37.7±10	3.02	2.9	
PEG@ Ti(Sm)O_2	-38.8±11	1.56	3.14	
CMC@ Ti(Sm)O_2	-42.6±13	4.08	3.10	

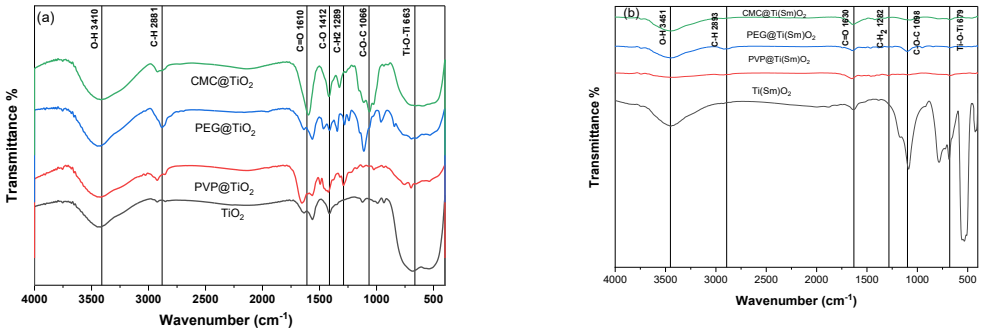

Fig. 3. FTIR spectra of (a) PVP@ TiO_2, PEG@ TiO_2, CMC@ TiO_2, (b) $Ti(Sm)O_2$, PVP $Ti(Sm)O_2$, PEG @$Ti(Sm)O_2$, and CMC @$Ti(Sm)O_2$ nanoparticles

in a decrease in the energy gaps, as indicated in Table 1. The lowest band gap was observed for $Ti(SmO_2)$, which indicates that doping Titanium oxides with Samarium reduces the band gap. This reduction in the band gap is attributed to the decreased recombination of electrons and holes, which enhances the charge transfer efficiency of the material. Overall, the UV/Vis absorbance spectra and the analysis of the band gaps provide insights into the electronic structure and optical properties of the synthesized TiO_2 nanoparticles, as well as the influence of Samarium doping and polymer coating on their energy gaps. The influence of different polymer coatings on the band gap of nanoparticles is complex and can vary depending on the specific polymers used. Factors such as the polymer's structure, functional groups, and interaction with the nanoparticles can affect the band gap. PVP is an electron-donating group can introduce energy states near the band edges, leading to a lower band gap. However, PEG with high dielectric constants or electron-withdrawing groups may have limited impact on the band gap or even increase it. CMC is a non-conductive polymer that does not significantly contribute to the energy levels within the band gap. Therefore, the coating of nanoparticles with CMC may not have a direct impact on the energy gap.

FTIR analysis

Infrared spectroscopy (FTIR) was employed to analyze the functional groups present in the synthesized compounds. Fig. 3 illustrates a series of FTIR spectra for TiO_2 and Samarium-doped TiO_2 nanoparticles, coated with PVP, PEG, and CMC. In the spectra, a prominent and strong band in the range of 580 to 660 cm^{-1} corresponds to the characteristic modes of TiO_2. This band provides evidence of the presence of TiO_2 in the samples. Additionally, an absorption range around 3427 cm^{-1} indicates the stretching vibrations of hydroxyl groups, which may be influenced by in-situ spectra recording and water reabsorption from the ambient atmosphere. Another absorption range around 1553 cm^{-1} is attributed to the bending vibrations of hydroxyl groups in molecular water. The clear peak observed at 1383 cm^{-1} is associated with the Ti-O modes, further confirming the presence of TiO_2. Furthermore, the FTIR spectrum of the coated TiO_2 nanoparticles is presented in Fig. 3. The absorbance observed in the range of 1066−1700 cm^{-1} corresponds to the vibrations of organic polymers. The appearance of new bands in this region is attributed to the existence of the organic polymer coating. For example, bands around 2881, 1352, and 1066 cm^{-1} represent the stretching vibrations of C-H bonds, the bending vibrations of C-H bonds, and the stretching vibrations of C-O bonds, respectively. The presence of these bands indicates the hydrogen-bonding nature and confirms the interaction between the organic polymer and the surface of TiO_2 and Samarium-doped TiO_2 nanoparticles. This interaction between the polymers and the nanoparticles further supports the successful coating process and providedes valuable information about the surface chemistry of the synthesized NPs.

Zeta potential

The zeta potential values of prepared nanoparticles sintered are shown in Fig.4. zeta potential has been utilized to be aware of the nature of prepared nanoparticle charges in DW. Zeta potential with a negative value ranging from -37.7 to -61.5 mV was obtained for the nanoparticle

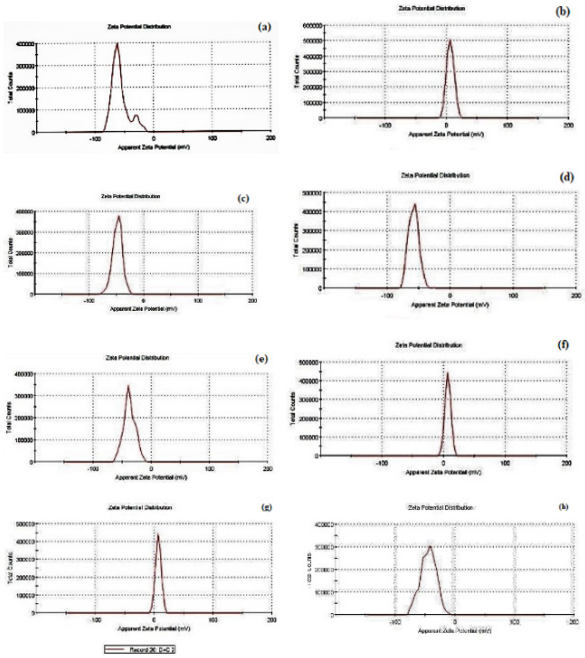

Fig. 4. Zeta potential for (a) TiO_2, (b) PVP@ TiO_2, (c) PEG@ TiO_2, (d) CMC @TiO_2, (e) Ti(Sm)O_2, (f) PVP @Ti(Sm)O_2, (g) PEG@Ti(Sm)O_2, (h) CMC @Ti(Sm)O_2 NPs

diluted in DW, corresponding to a stable colloidal without particle settlement. Zeta potential lowered as the NPS was coated with polymers, as in Fig. 5. When nanoparticles are coated with polymers such as PVP (polyvinylpyrrolidone), PEG (polyethylene glycol) and CMC (carboxymethyl cellulose), the zeta potential of the nanoparticles can become lower or even approach zero [30]. This is because the polymer coating can shield the surface charges of the nanoparticles, reducing their electrostatic interactions with the surrounding medium. The difference in zeta potential between PEG@TiO_2 and PVP@TiO_2 nanoparticles is attributed to the solvation properties of the polymers. PEG forms a dense hydration layer around the nanoparticles due to its strong solvation properties in water, leading to a more negative zeta potential. In contrast, PVP has less pronounced solvation effects, resulting in a less dense hydration layer and a slightly less negative zeta potential for PVP@TiO_2 nanoparticles. Therefore, the exact effect of polymer coatings on the zeta potential of nanoparticles can vary depending on the specific experimental conditions. Moreover, the prepared suspension endorsed with general zeta potential (ξ) value of 30 mV with a positive or negative sign for better stability. Lower values of Zeta potential suggest aggregation of nanoparticles due to Van der Waals forces. Zhang et al. confirmed the measurement of the zeta potential of the material to understand the nature of cellular interaction, cellular diagnostics, and therapeutics of normal and cancer cell effects.

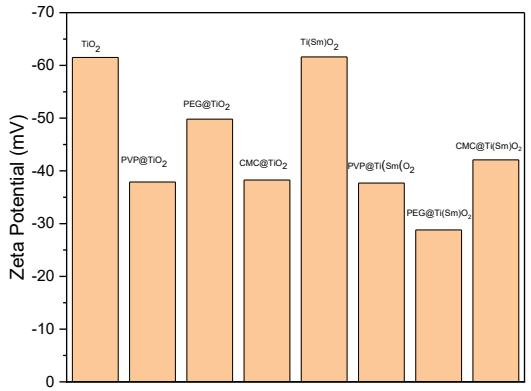

Fig. 5. Zeta potential distribution of TiO_2, PVP@TiO_2, PEG@ TiO_2, CMC@ TiO_2, Ti(Sm)O_2, PVP@ Ti(Sm)O_2, PEG @Ti(Sm)O2, and CMC@ Ti(Sm)O_2 NPS

Transmission electron microscope (TEM)

TEM of TiO_2, Ti(SmO_2) NPs, declared a spherical morphology and a comparably narrow size dispersion characteristic of the hydrothermal method. The particle size distribution histogram was outlined regarded the counted ten nanoparticles as shown in Fig. 6. The mean particle size is 70 nm with a 23.59 nm standard deviation. The particle size distribution histogram was

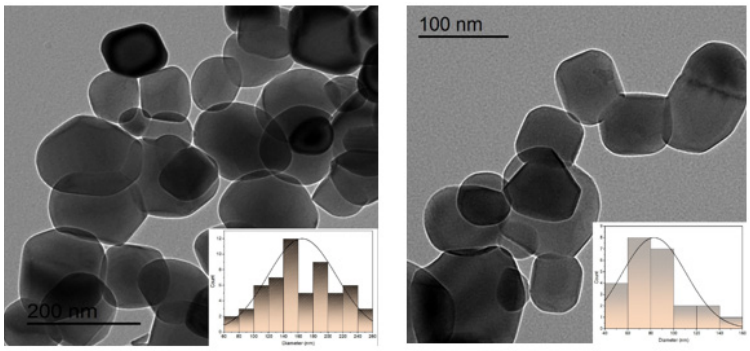

Fig. 6. (a) TEM of TiO_2 nanoparticles and the corresponding particle size distribution histogram, (b) TEM of $Ti(Sm)O_2$ and the corresponding particle size distribution histogram

outlined regarded to the counted ten nanoparticles. The mean particle size of $Ti(SmO_2)$ is 83 nm with a 22.30 nm standard deviation.

As an indirect band gap semiconductor, TiO_2 shows no band gap photoluminescence. Photoluminescence (PL) arises from recombining oppositely charged trapped and free carriers. Photoluminescence from $Ti(Sm)O_2$ suspension contains a band at 600 nm and a band at around 515 nm. The band at 600 nm exhibits a strong correlation with defects, and the 515 nm band shows a close relationship with the oxygen vacancies. A series of $Ti(Sm)O_2$ PL studies in different coated samples in Figyre 7. The normal emission of nanoparticles is dominated by PL arising from the recombination of trapped electrons with valence band holes, leading to a broad spectrum with a peak in 600 nm. There may also be a higher energy emission originating from recombining mobile electrons with trapped holes. Because both types of recombination depend on the spatial coincidence of trapped and roaming charges, comparing the energy gaps and conductivity values (Fig. 2, Table 1) with PL obtained from prepared samples, we can conclude that the PL intensity is greater when transport is hindered, and lower when the charges are more mobile. The influence of polymer molecular weight on emission intensity is complex and depends on various factors, including nanoparticle size, surface properties, and the presence of additional additives. Higher molecular weight polymers can enhance emission intensity by improving nanoparticle stability and reducing aggregation, thereby preventing energy transfer processes that lead to emission quenching. On the other hand, lower molecular weight polymers may promote closer contact between nanoparticles, resulting in enhanced energy transfer and potentially higher emission intensity. However, it is important to note that the relationship between polymer molecular weight and emission intensity is not solely determined by molecular weight, but also by the specific properties of the polymer and its interaction with the nanoparticles. In the case of $CMC@Ti(Sm)O_2$, the observed reduction in photoluminescence (PL) peaks could be attributed to factors such as changes in surface properties or the influence of CMC on energy transfer processes.

Phenotypic characterization of PBMCs

The characterization of PBMCs using flow cytometry provides valuable insights into the cellular composition and enables a more detailed investigation of immune responses and functions in the context of our study. In passage three, we characterized peripheral blood mononuclear

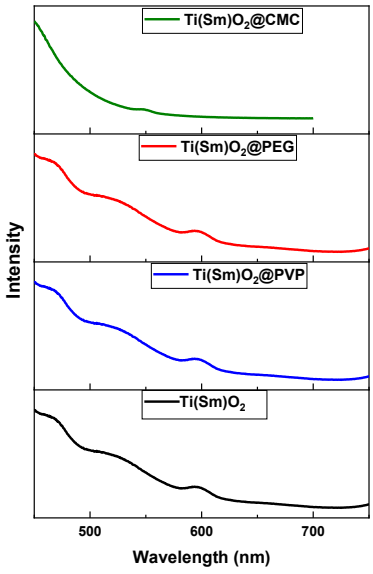

Fig. 7. Photoluminescence of $Ti(Sm)O_2$, PVP $Ti(Sm)O_2$, PEG @ $Ti(Sm)O_2$, and CMC @$Ti(Sm)O_2$ nanoparticles

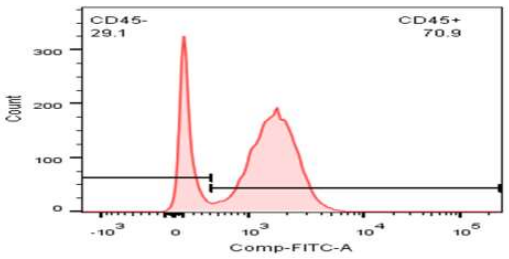

Fig. 8. CD 45 FTIC mouse anti-human using flow cytometry

cells (PBMCs) using flow cytometric analysis. The flow cytometry results demonstrated that a significant proportion of PBMC cells expressed the hematopoietic marker CD45, with a percentage of 70.9% (Fig. 8). This finding indicates that the isolated PBMC population consisted predominantly of hematopoietic cells, as expected. CD45 is a common marker for hematopoietic cells, including lymphocytes, monocytes, and granulocytes, and its expression confirms the presence of these cell types within the PBMC population. The flow cytometric analysis allowed for the identification and quantification of specific cell populations based on their surface marker expression. In this case, the positive expression of CD45 in the majority of PBMC cells suggests the presence of immune cells, which is consistent with the composition of PBMCs. These results further support the suitability of PBMCs for downstream functional and phenotypic studies, as they represent a heterogeneous population of immune cells.

Human mononuclear cell culture and treatment protocol

The morphological microstructure (100×) is observed using an Olympus IX51inverted fluorescence microscope. Recording the viability for each plate after 90 min, as shown in Fig. 9, shows the viability for the mononuclear cells after incubation with NPs in the dilatation (1NPs:1cells), (1NPs:3cells), (1NPs:5cells). Cell viability results ensure TiO_2, PVP @TiO_2, PEG @TiO_2, CMC@TiO_2, Ti(Sm)O_2, PVP@ Ti(Sm)O_2, PEG@ Ti(Sm)O_2, and CMC@ Ti(Sm)O_2 NPS is blood biocompatibility, so it will be completely safe within few hours before any interaction with blood cells occurs. The blood biocompatibility of our synthesized NPS may relate to its surface nature.

After injecting a dose of nanoparticles (0.1 ml), rats were dissected and subjected to hematoxylin and eosin (H&E) examination at 1 hr and 6 days post-injection (Fig. 10). The H&E

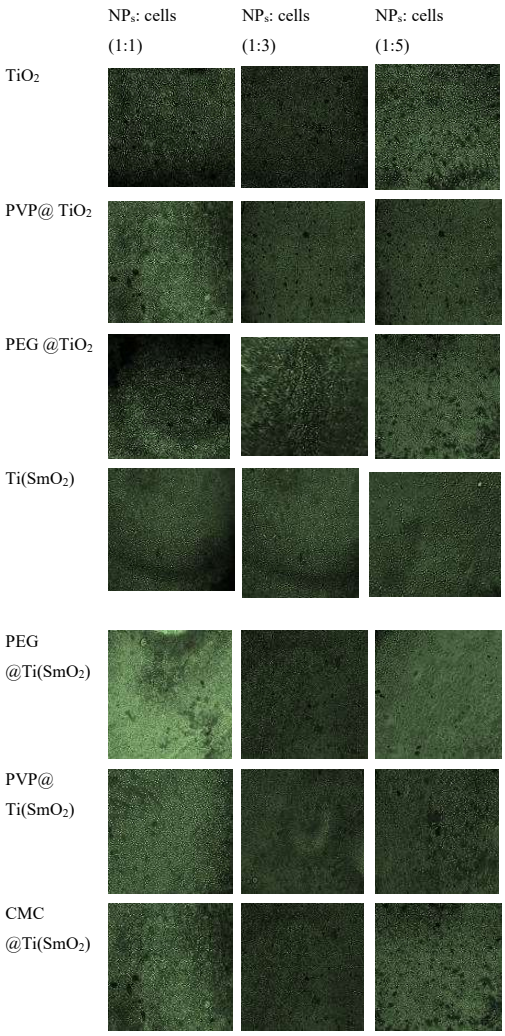

Fig. 9. The mononuclear cells after incubation with NPs after 90 min

examination results at 1 hr showed that most of the nanoparticles accumulated in the lung. However, no adverse effects of the nanoparticles were observed in the pancreas, heart, lung, or kidney. Nonetheless, variable levels of injuries were observed in the lung, liver, and heart, depending on the nature of the injected nanoparticles. In the lung samples taken after 1 hr, diffuse alveolar damage (DAD) was observed. DAD is characterized by congested lung vessels, interstitial hemorrhage and fibrosis, interstitial neutrophils, bloody exudates in the alveoli, pulmonary congestion, bronchiolar epithelial damage, and hemosiderin-laden macrophages. In the liver, mild portal inflammation and little bile duct proliferation were observed in samples injected with nanoparticles, except for TiO_2 coated with PVP, which showed minimal portal inflammation and no bile duct

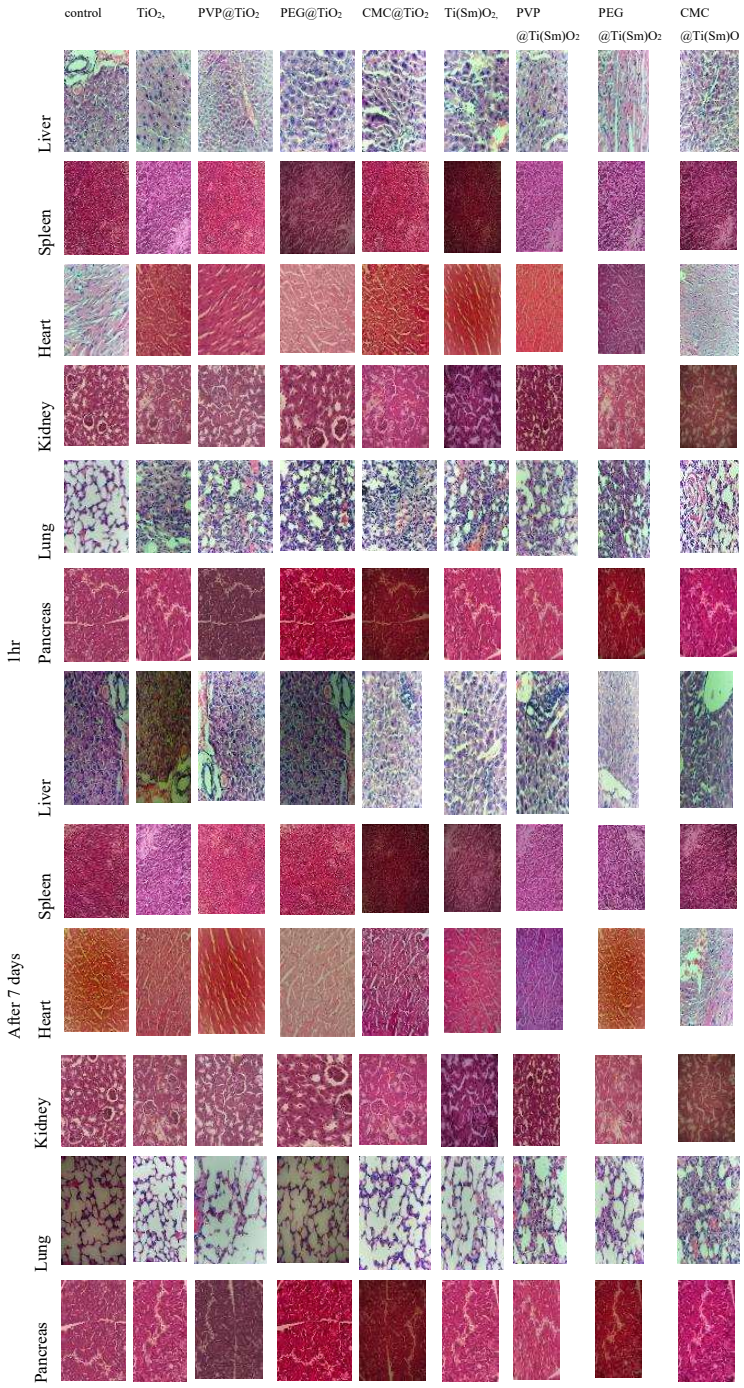

Fig. 10. Histological examination of heart, liver, Lung, Pancreas, kidney, and spleen injected by 0.1 ml saline and Nanoparticles followed by dissection after 1 hr and 7 days, sections were stained with H&E and observed under the light microscope at 400x magnifaction

proliferation. Hepatocyte degeneration (pyknotic) was observed in zone 1, 2, and 3 of the liver for TiO_2. TiO_2 @ CMC and $Ti(SmO)_2$ @ PVP exhibited hepatocyte degeneration and injury in zone 2 and 3. TiO_2 @ PVP and $Ti(SmO)_2$ showed hepatocyte degeneration and injury in zone 3. TiO_2 coated with PEG showed scattered spotty necrosis in hepatocytes in zone 3. However, no hepatocyte injury was found in $Ti(SmO)_2$ @ PEG and $Ti(SmO)_2$ @ CMC. To assess the long-term toxicity of the nanoparticles, histological examination was conducted on several organs, including the heart,

Table 2. Toxological effect on serum levels of ALT, AST, creatinine.

After 1 hr	Creatinine (U/L)	ALT (U/L)	AST (U/L)
Control	0.15	22	110
TiO_2	0.27	47	516
PVP@TiO_2	0.29	57	671
PEG@TiO_2	0.26	39	310
CMC@TiO_2	0.25	45	305
Ti(Sm)O_2	0.25	40	480
PVP@ Ti(Sm)O_2	0.24	56	620
PEG@ Ti(Sm)O_2	0.23	63	588
CMC@ Ti(Sm)O_2	0.24	50	638
After 7 days			
TiO_2	0.25	30	220
PVP@TiO_2	0.28	26	229
PEG@TiO_2	0.24	24	145
CMC@TiO_2	0.23	24	130
Ti(Sm)O_2	0.24	28	163
PVP@ Ti(Sm)O_2	0.23	30	177
PEG@ Ti(Sm)O_2	0.24	29	176
CMC@ Ti(Sm)O_2	0.16	23	260

liver, lung, pancreas, kidney, and spleen after seven days. H&E examination revealed no adverse effects of the nanoparticles on the heart, pancreas, kidney, and spleen. Fortunately, the lung showed complete resolution for TiO_2, PEG@ TiO_2, CMC @TiO_2, Ti(Sm)O_2, PVP @Ti(Sm)O_2 nanoparticles. Serum levels of alanine aminotransferase (ALT), aspartate aminotransferase (AST), and creatinine (Cr) were measured after 1 hr and seven days to evaluate liver and kidney function. After 1 hr, ALT levels indicated minimal liver toxicity, while creatinine levels indicated normal kidney function. Toxicological effects on serum levels of ALT, AST, and Creatinine are shown in Table 2. However, AST levels were higher. After seven days, ALT and AST levels indicated minimal liver toxicity, and creatinine levels indicated normal kidney function. Based on the biodistribution of TiO_2 nanoparticles, they can potentially be developed as target-specific agents for lung-related pathologies, allowing for the selective distinction of lung diseases.

X-ray CT phantom images were captured

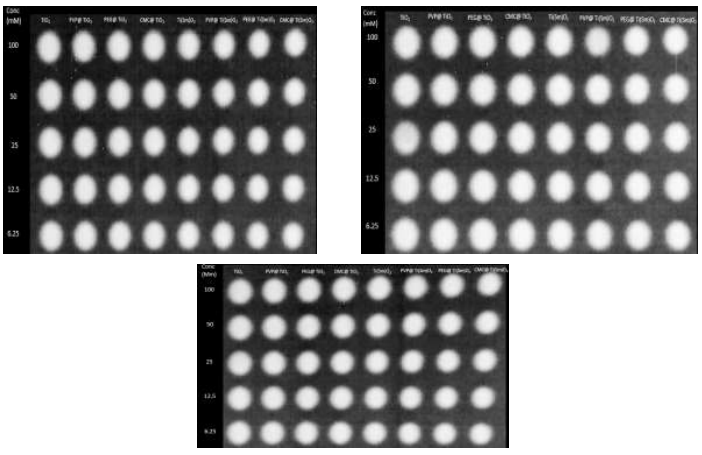

Fig. 11. CT phantom images of TiO_2, PVP@TiO_2, PEG@TiO_2, and CMC@TiO_2 nanoparticles b UV spectra of Ti(Sm)O_2, PVP@Ti(Sm)O_2, PEG@Ti(Sm)O_2, and CMC@Ti(Sm)O_2 nanoparticles

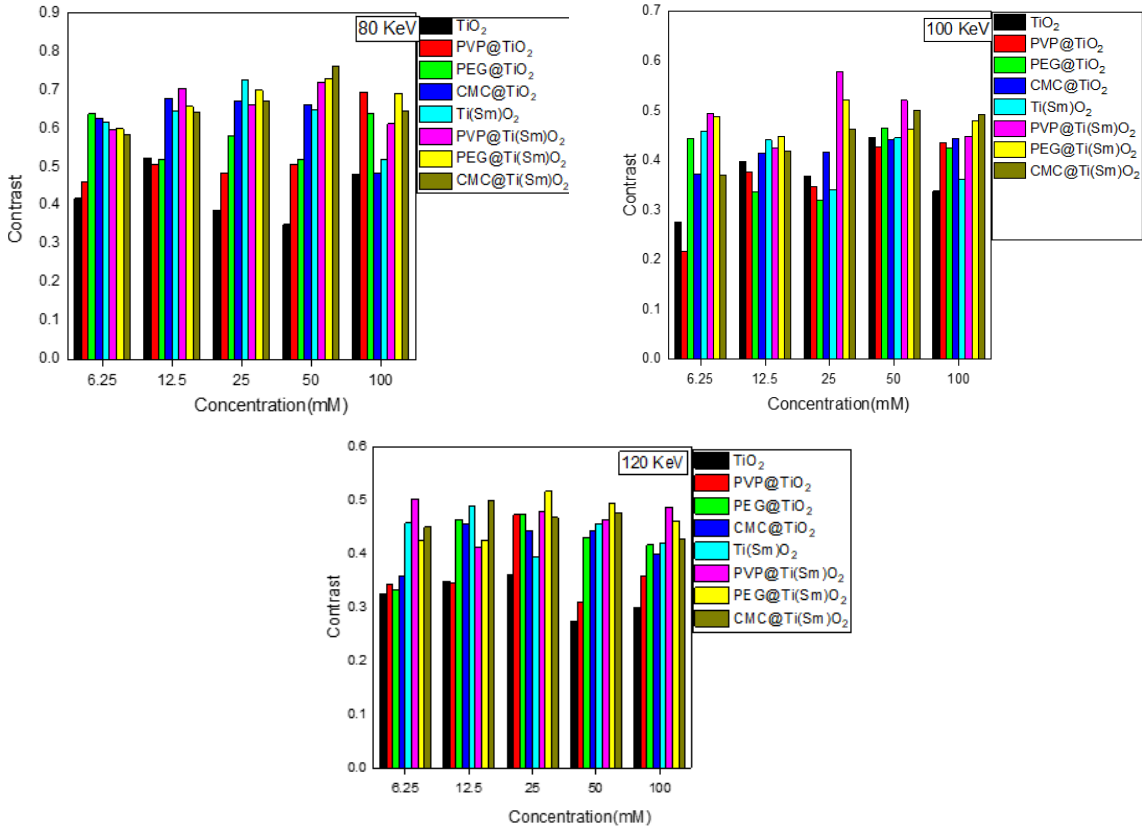

Fig. 12. The CT number indicating the contrast of TiO_2, $Ti(SmO_2)$ coated with PEG, CMC, PVP a) 80 Kv b)100 Kv c)120 Kv

using various concentrations of TiO_2 and Ti(Sm) O_2 coated with various polymers diluted with distilled water Fig. 11. The CT number increased as the concentration of nanoparticles increased Fig. 12. The variation, in contrast, is slightly varied. However, the high contrast was gained at 80 Kv.

CONCLUSION

The synthesis and characterization of Samarium-doped TiO_2 nanoparticles (Ti(Sm)O_2 NPs) coated with PVP, PEG, and CMC have been successfully conducted in this study. The results demonstrated the desirable properties of these nanoparticles, including their morphology, crystal structure, optical properties, surface charge, and biocompatibility. *In vivo* imaging evaluations revealed their excellent imaging capabilities, particularly in distinguishing lung pathologies, making them highly promising for targeted imaging applications. Furthermore, in vivo toxicity studies demonstrated the biocompatibility and safety of the nanoparticles, indicating their potential for clinical translation. The nanoparticles exhibited a high accumulation in the lung, which is advantageous for lung-specific targeting in disease diagnosis and treatment. The presence of diffuse alveolar damage (DAD) observed in the early stages was found to resolve over time, indicating the transient nature of the nanoparticle-induced effects. Overall, the synthesized Ti(Sm) O_2 nanoparticles coated with PVP, PEG, and CMC hold great potential for advanced imaging techniques and targeted imaging applications. Their enhanced stability, biocompatibility, and excellent imaging capabilities make them valuable tools for the diagnosis and monitoring of various lung pathologies. These nanoparticles offer opportunities for improved treatment outcomes, patient care, and the development of advanced contrast agents for biomedical applications.

ACKNOWLEDGMENTS

No fund.

ETHICS APPROVAL AND CONSENT TO PARTICIPATE

Animal studies were performed in MERC accredited facility under the approval of Faculty of medicine, Mansoura University.

CONSENT FOR PUBLICATION

Not applicable.

AVAILABILITY OF DATA AND MATERIALS

The data sets used and/or analysed during this study are available from the corresponding author upon reasonable request.

CONFLICTS OF INTEREST

The authors declare that they have no conflict of interests.

REFERENCES

1. Bae KH, Chung HJ, Park TG. Nanomaterials for cancer therapy and imaging. Molecules and cells. 2011;31(4):295-302.
2. Hallouard F, Anton N, Choquet P, Constantinesco A, Vandamme T. Iodinated blood pool contrast media for preclinical X-ray imaging applications--a review. Biomaterials. 2010;31(24):6249-6268.
3. Liu Y, Ai K, Lu L. Nanoparticulate X-ray computed tomography contrast agents: from design validation to in vivo applications. Accounts of chemical research. 2012;45(10):1817-1827.
4. Cormode DP, Naha PC, Fayad ZA. Nanoparticle contrast agents for computed tomography: a focus on micelles. Contrast media & molecular imaging. 2014;9(1):37-52.
5. Hainfeld JF, Slatkin DN, Focella TM, Smilowitz HM. Gold nanoparticles: a new X-ray contrast agent. Br J Radiol. 2006;79(939):248-253.
6. Jackson PA, Rahman WN, Wong CJ, Ackerly T, Geso M. Potential dependent superiority of gold nanoparticles in comparison to iodinated contrast agents. EMJ Radiol. 2010;75(1):104-109.
7. Connor EE, Mwamuka J, Gole A, Murphy CJ, Wyatt MD. Gold nanoparticles are taken up by human cells but do not cause acute cytotoxicity. Small (Weinheim an der Bergstrasse, Germany). 2005;1(3):325-327.
8. Jakhmola A, Anton N, Vandamme TF. Inorganic nanoparticles based contrast agents for X-ray computed tomography. Advanced healthcare materials. 2012;1(4):413-431.
9. Rabin O, Manuel Perez J, Grimm J, Wojtkiewicz G, Weissleder R. An X-ray computed tomography imaging agent based on long-circulating bismuth sulphide nanoparticles. Nature materials. 2006;5(2):118-122.
10. Pan D, Roessl E, Schlomka JP, Caruthers SD, Senpan A, Scott MJ, et al. Computed tomography in color: NanoK-enhanced spectral CT molecular imaging. Angewandte Chemie. 2010;122(50):9829-9833.
11. Nadel JA, Wolfe WG, Graf PD, Youker JE, Zamel N, Austin JH, et al. Powdered tantalum. N Engl J Med. 1970;283(6):281-286.
12. Chakravarty S, Hix JML, Wiewiora KA, Volk MC, Kenyon E, Shuboni-Mulligan DD, et al. Tantalum oxide nanoparticles as versatile contrast agents for X-ray computed tomography. Nanoscale. 2020;12(14):7720-7734.
13. Xing H, Bu W, Ren Q, Zheng X, Li M, Zhang S, et al. A NaYbF4: Tm3+ nanoprobe for CT and NIR-to-NIR fluorescent bimodal imaging. Biomaterials. 2012;33(21):5384-5393.
14. Jafari S, Mahyad B, Hashemzadeh H, Janfaza S, Gholikhani T, Tayebi L. Biomedical Applications of TiO(2) Nanostructures: Recent Advances. Int J Nanomed. 2020;15:3447-3470.
15. Townley HE, Rapa E, Wakefield G, Dobson PJ. Nanoparticle augmented radiation treatment decreases cancer cell proliferation. Nanomedicine: nanotechnology, biology, and medicine. 2012;8(4):526-536.
16. Michalet X, Pinaud FF, Bentolila LA, Tsay JM, Doose S, Li JJ, et al. Quantum dots for live cells, in vivo imaging, and diagnostics. Science (New York, NY). 2005;307(5709):538-544.
17. Koudrina A, DeRosa MC. Advances in Medical Imaging: Aptamer- and Peptide-Targeted MRI and CT Contrast Agents. ACS omega. 2020;5(36):22691-22701.
18. Fahmy HM, Mosleh AM, Elghany AA, Shams-Eldin E, Abu Serea ES, Ali SA, et al. Coated silver nanoparticles: synthesis, cytotoxicity, and optical properties. RSC advances. 2019;9(35):20118-20136.
19. Abo Gabal R, Osama S, Hanafy N, Oraby A. Micellization thermodynamics as a function of the temperature of a cationic zwitterionic dodecyl phosphocholine and anionic sodium dodecyl sulfate mixed micelles with fluorometry. Appl Phys A. 2023;129(3):201.
20. Park JY, Daksha P, Lee GH, Woo S, Chang Y. Highly water-dispersible PEG surface modified ultra small superparamagnetic iron oxide nanoparticles useful for target-specific biomedical applications. Nanotechnology. 2008;19(36):365603.
21. Gaaz TS, Sulong AB, Akhtar MN, Kadhum AA, Mohamad AB, Al-Amiery AA. Properties and Applications of Polyvinyl Alcohol, Halloysite Nanotubes and Their Nanocomposites. Molecules (Basel, Switzerland). 2015;20(12):22833-22447.
22. Babic M, Horák D, Trchová M, Jendelová P, Glogarová K, Lesný P, et al. Poly(L-lysine)-modified iron oxide nanoparticles for stem cell labeling. Bioconjugate chemistry. 2008;19(3):740-750.
23. Mano SS, Kanehira K, Sonezaki S, Taniguchi A. Effect of polyethylene glycol modification of TiO_2nanoparticles on cytotoxicity and gene expressions in human cell lines. Int J Mol Sci. 2012;13(3):3703-3717.
24. Vitha MF. Spectroscopy: Principles and Instrumentation: John Wiley & Sons; 2018;Ch.2:39.
25. Kannan M. Transmission Electron Microscope -Principle, Components and Applications Illumination system (Electron gun and condenser lenses) Electron gun. 2018. p. 93-101.
26. Franks GV. Zeta potentials and yield stresses of silica suspensions in concentrated monovalent electrolytes: isoelectric point shift and additional attraction. J Colloid Interface Sci. 2002;249(1):44-51.
27. De Dios I, Ramudo L, Alonso JR, Recio JS, Garcia-Montero AC, Manso MA. CD45 expression on rat acinar cells: involvement in pro-inflammatory cytokine production. FEBS letters. 2005;579(28):6355-6360.
28. Gabal RA, Shokeir D, Orabi A. Cytotoxicity and Hemostatic One Step Green Synthesis of Iron Nanoparticles Coated with Green Tea for Biomedical Application. Trends Sci. 2022;19(3):2062.
29. Pogson EM, McNamara J, Metcalfe P, Lewis RA. Comparing and evaluating the efficacy of the TOR18FG Leeds test X-ray phantom for T-rays. Quantitative imaging in medicine and surgery. 2013;3(1):18-27.
30. Shi J, Votruba AR, Farokhzad OC, Langer R. Nanotechnology in drug delivery and tissue engineering: from discovery to applications. Nano letters. 2010;10(9):3223-3230.